Monthly Notices of the ROYAL ASTRONOMICAL SOCIETY

MNRAS **506,** 2170–2180 (2021) https://doi.org/10.1093/mnras/stab1857
Advance Access publication 2021 July 2

Interaction of the galactic-centre super bubbles with the gaseous disc

Yoshiaki Sofue[1]★ and Jun Kataoka[2]★

[1]*Institute of Astronomy, The University of Tokyo, Mitaka, Tokyo 181-0015, Japan*
[2]*Faculty of Science and Engineering, Waseda University, Shinjyuku, Tokyo 169-8555, Japan*

Accepted 2021 June 25. Received 2021 June 21; in original form 2021 February 25

ABSTRACT

The interaction of Galactic centre (GC) super bubbles (GSBs) with the gaseous disc and halo of the Milky Way is investigated using radio continuum, X-ray, H I, and CO line surveys. The radio North Polar Spur (NPS) constitutes the brightest eastern ridge of GSB, brightening towards the galactic plane and reaching $l = 22^\circ$, $b = +2^\circ$ at the sharpest end, where it intersects the tangential direction of the 3-kpc-expanding ring and crater. Examination of the spur ridges reveals that the entire GSB, including the NPS and its counter spurs, constitutes a GC-symmetrical Ω/ ʊ shape. The thickness and gas density of the H I and CO discs are shown to increase sharply from the inside (lower longitude) to the outside the 3-kpc crater. Formation of crater is explained by the sweeping of the upper layer of disc gas by the shock wave from the GC by the explosion ∼10 My ago with the emitted energy of several 10^{55} erg. Based on the discussion, a unified view on the structure and formation mechanism of GSB is presented.

Key words: ISM: individual objects: North Polar Spur – ISM: shock wave – ISM: bubbles – Galaxy: centre – galaxies: individual: objects (the Milky Way).

1 INTRODUCTION

The Galactic centre (GC) exhibits a variety of explosive phenomena, associated with high-energy outflows and shock waves. The most energetic and gigantic shock wave so far reported is the GC super bubbles (GSBs)[1] due to a nuclear explosion with released energy on the order of $\sim 10^{55-56}$ erg and extent as large as $\sim \pm 10$ kpc above and below the Galactic plane (Sofue 1977, 2000; Bland-Hawthorn & Cohen 2003; Crocker et al. 2015; Sofue et al. 2016; Sarkar et al. 2015; Kataoka et al. 2018). In this paper, we revisit this prominent object in the Galaxy in view of the GC explosion model, being inspired by the recent excellent X-ray observations of the whole sky with the eROSITA (Predehl et al. 2020).

High-altitude, large-scale bubbles in the halo around the GC have been evidenced in the last decades by the all sky surveys in radio continuum emission (Haslam et al. 1982; Reich, Testori & Reich 2001; Planck collaboration IX 2013), X-rays (Snowden et al. 1997; Predehl et al. 2020), and γ-rays (Su, Slatyer & Finkbeiner 2010), although their scale size and morphology differ in different energy bands. Moreover, giant magnetized outflows from the GC are also suggested by linear polarization measurement in radio band (Carretti et al. 2013).

The bipolar double-horn structure has been interpreted as a shock wave from the GC, and is well simulated by the bipolar-hyper shell model (Sofue 1994, 2000; Guo & Mathews 2012; Sofue et al. 2016; Sarkar et al. 2015; Sarkar 2019). The connection of the GSB to the energetic phenomena in the GC has been firmly confirmed by the discovery of the *Fermi* bubbles (Su et al. 2010; Crocker et al. 2015; Kataoka et al. 2018). In fact, various outflow phenomena have been known in the GC region, such as the GC lobe (Sofue & Handa 1984) as recently revealed of its vertical connection to higher latitude halo (Heywood et al. 2019). An X-ray chimney extending hundreds of parsecs above and below the GC has been discussed with tight correlation with the radio and infrared (IR) vertical structures (Nakashima et al. 2013; Ponti et al. 2019; Ponti et al. 2021). Disturbed ionized gas appears to be flowing out at high speed from the GC into the halo below the galactic plane Savage et al. (2017). These observations seem to connect Sgr A to the *Fermi* bubbles, further corroborating the GC-origin scenario of the outer bubbles. Interconnections and coherent features in radio, IR, X-ray, and γ-ray maps are thus suggested in the central few degrees of the GC to ∼10 kpc of the Galactic halo in the past ∼10−20 My.

Fig. 1 summarizes the starburst or GC explosion model (Sofue 2000; Sofue et al.2016), which considered the shock wave propagation in the disc and halo, as compared to the X-ray all-sky maps. The top panel shows comparison of the model with the *ROSAT* all-sky map (Snowden et al. 1997), where the interstellar absorption is calculated for a disc model of neutral gas. The middle panel shows a simulated three-colour X-ray image in the 0.25, 0.75, and 2 keV compared with the eROSITA observation for the inner region of GSB (Predehl et al. 2020). The interstellar absorption has been corrected for using the H I survey data (Kalberla et al. 2005). The simulations well reproduce the observed X-ray morphology of GSB and the increasing absorption and hardening of the spectrum towards the Galactic plane.

Besides the bubbles and outflows, a giant H I hole has been known around the GC, which composes a bipolar conical cavity of neutral gas and is supposed to have been blown off by a galactic wind (Lockman 1984; Lockman & McClure-Griffiths 2016). The H I hole has its root in the Galactic plane, coinciding with the 3-

★ E-mail: sofue@ioa.s.u-tokyo.ac.jp (YS); kataoka.jun@waseda.jp (JK)
[1]The same object has been given various names such as radio loops, Galactic super bubbles, bipolar hyper shells (BHS), *ROSAT*/eROSITA bubbles, etc.

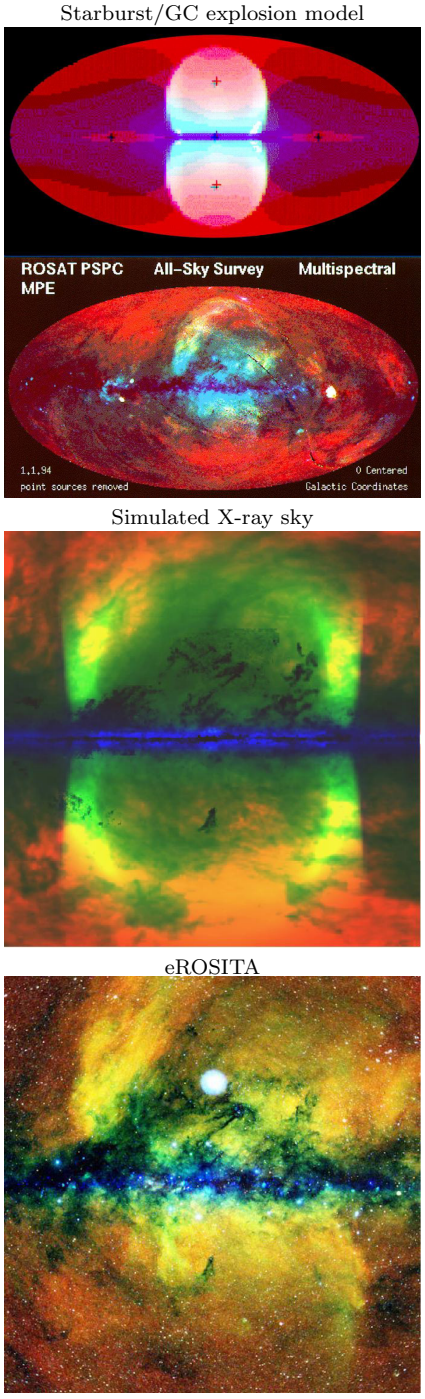

Figure 1. Summary of the bipolar hyper-shell model. [Top] Calculated X-ray sky (Sofue 2000) compared with the *ROSAT* all sky X-ray map (Snowden et al. 1997). RGB colors stand for 1/4, 3/4, and 1.5 keV, respectively. For intensities see the cited papers. [Middle] Simulated X-ray map on the $100^\circ \times 100^\circ$ sky (RGB for 0.25, 0.75, and 2 keV in arbitrary intensity scaling) corrected for extinction (Sofue et al. 2016) using the H I survey data (Kalberla et al. 2005). [Bottom] eROSITA RGB map of the central $100^\circ \times 100^\circ$ region (Predehl et al. 2020) as reproduced from url https://www.mpe.mpg.de/7461761/news20200619. Note the significant absorption near the galactic plane, where the radio data are crucial in order to see the interaction of the spurs with the disc.

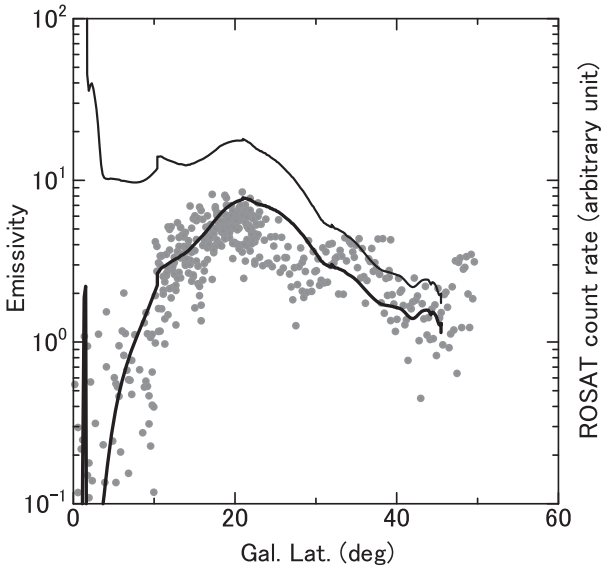

Figure 2. *ROSAT* X-ray count rates at 0.75 keV along the NPS in arbitrary unit by the dots (Snowden et al. 1997) compared with the intrinsic emissivity along the post-shock from simulation of the starburst model by the thin line (Sofue et al. 2016), and with that after correction for the interstellar extinction due to the galactic disc by the thick line. Compare the relative latitudinal variations, as the absolute values are arbitrary.

kpc-expanding ring (Sanders & Prendergast 1974; Cohen & Davies 1976; Bania 1980). The cylindrical boundary of the H I hole makes a crater-like structure of radius 3 kpc around the GC, whose tangential directions coincides with the roots of the North Polar Spur (NPS) and its counter spurs (Sofue 2017).

The NPS is the most prominent spur in the galactic halo in radio (Haslam et al. 1982) and soft X-rays (Snowden et al. 1997; Predehl et al. 2020). The radio NPS emerges from the galactic plane at G22+02 (Sofue & Reich 1979), where the spur exhibits maximum brightness and the sharpest cross-section. This position exactly coincides with the tangential direction of the 3-kpc-expanding ring in H I and CO lines (Sofue 2017).

Energetic events in the GC associated with giant bubbles and shock waves, thus exhibit various foot prints in the halo and disc from neutral ISM to high-energy emissions. In this paper, we re-examine the morphological correlation between the 3-kpc crater and the GSB, looking for further evidence of the GC explosion in the H I and molecular discs using radio continuum, X-ray, H I, and CO line surveys. We, then, attempt to give a comprehensive explanation for various diverse features observed over the wide range of spectrum.

2 X-RAY GSB ABSORBED BY THE DISC

2.1 Extinction of X-ray spurs by the galactic disc

The top panels of Fig. 1 demonstrate the heavy extinction of the X-rays from the GC and halo by the galactic disc. Fig. 2 shows the latitudinal variation of the X-ray intensity at 0.75 keV as observed by *ROSAT* (Snowden et al. 1997). The X-ray intensities along the spurs are significantly depressed at latitudes lower than $|b| \lesssim 10^\circ$. Such depression can be understood as due to the following two kinds of bounded features at low latitudes.

(a) Absorption-bounded cut due to interstellar extinction by heavy elements, whose optical depth is proportional to the line-of-sight

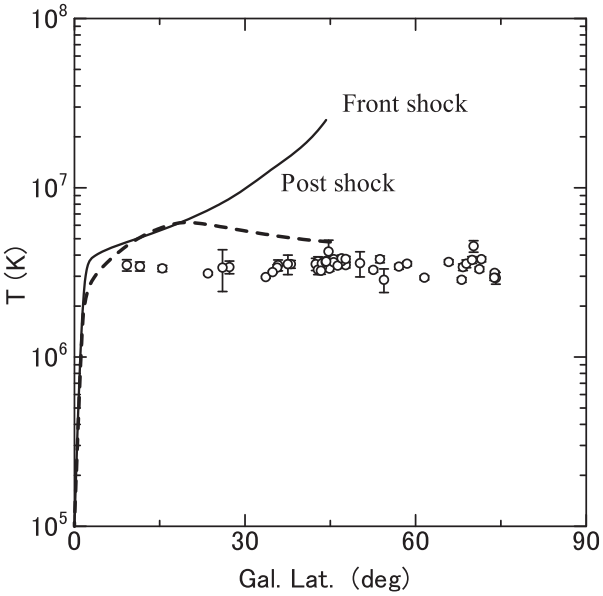

Figure 3. Gas temperature against latitude (=atan(z/8 kpc)) at the front shock (the full line) and post-shock (the dashed line) from simulation of the starburst model, compared with observed X-ray temperatures from SUZAKU (the circles; Kataoka et al. 2013; Tahara et al. 2015; Akita et al. 2018) and HaloSat (LaRocca et al. 2020).

depth of the disc obeying the sec $|b|$ law (Sofue 1994, 2015; Lallement et al. 2016; Fig. 2). This cut occurs at $|b| < \sim 10^\circ - 20^\circ$ by the local H I disc.

(b) Emission-bounded cut due to suppression of the intrinsic emissivity at low latitudes according to decreasing temperature in the galactic disc, where neutral gas is dominant at temperatures below $< \sim 10^4$ K as predicted by simulations (Sofue et al. 2016; Fig. 3). This cut occurs at altitudes as low as $|z| \sim <200$ pc, or $|b| < \sim 2^\circ$, which is difficult to detect even it is present because of the strong absorption by the foreground disc gas as above.

In either case, the observed apparent cut-off soft X-ray brightness near the galactic plane makes contrast to the continuous radio continuum ridge of the NPS intersecting the disc.

The latitudinal variation of the X-rays due to interstellar extinction has been calculated using the hydrodynamical simulation as shown in Fig. 1. Fig. 2 compares the expected variation of intrinsic emissivity along the simulated post-shock (the densest inner shell of the simulation) by a thin line with that after correction for the interstellar extinction by a thick line. Here, the galactic disc is expressed by a plane-parallel gas layer of thickness of 100 pc having absorption coefficient of 5×10^{-3} pc^{-1}, or $\tau = 1$ by 200 pc in the galactic plane. We plot the observed *ROSAT* intensities along the NPS by the grey dots, which are well fitted by the simulation with the disc extinction.

From the strongly extinct nature near the Galactic plane as proved by Figs 1 and 2, we may argue that the X-ray maps are not appropriate for studying the physics of GSB interacting with the disc.

2.2 Temperature variation with height

On the other hand, X-ray maps at high latitudes may be used to represent and study various physical properties of the GSB. Fig. 3 shows gaseous temperature along the NPS plotted against the galactic latitude as observed with SUZAKU (Kataoka et al. 2013; Tahara et al. 2015; Akita et al. 2018), and HaloSat (LaRocca et al. 2020). In all the data plotted here, the X-ray spectra are modelled by a same three-component plasma model: APEC1 + Wabs × (APEC2 + PL), where Wabs represents the Galactic absorption, APEC1 is an unabsorbed thermal component that represents the Local Bubble emission, APEC2 is an absorbed thermal component that represents the shocked halo gas like NPS, and PL is the contribution from cosmic X-ray background. Note that the temperature of APEC2 is nearly constant at $kT \sim 0.3$ keV, or $T \sim 3 \times 10^6$ K [(but see a slight different version of model fitting in which APEC2 is further divided into $kT \simeq 0.2$ and 0.4 keV components corresponding to unshocked and shocked halo gass (Miller & Bregman 2016)]. According to the bipolar-hypershell model, the high temperature can be reasonably attributed to heating of the halo gas by explosive event in the GC associated with a giant shock wave expanding at $\sim 200-300$ km s^{-1} (Sofue 1980; Sofue et al. 2016; Sarkar 2019; Zhang & Guo 2020).

According to the simulation near the Galactic plane at $z < \sim 0.2$ kpc, the temperature is expected to be significantly lower than that in the halo due to the stronger deceleration of the shock wave inside the disc, causing decrease in the temperature, and so the cooling rate and emissivity of X-rays (Fig. 3). However, the current X-ray observations cannot observe the intrinsic behaviour at lower latitudes than $|b| \leq 10^\circ$ because of the strong absorption by the foreground galactic disc as in Fig. 2.

As shown in Fig. 3, observed X-ray gas temperature of $kT \simeq 0.3$ keV is surprisingly uniform in the halo against latitude, and is roughly consistent with the 'post-shock' temperature predicted from the simulation of the starburst origin model.

On the other hand, temperature of 'front shock' is generally much higher. In fact, MHD simulation predicts that the shock velocity gets even faster, sometimes more than $\simeq 1000$ km s^{-1}, or $kT \simeq 1$ keV at high b owing to substantial decrease of the halo gas density where the shock propagates. Note that the cooling time-scale of the X-ray-emitting gas is expressed as

$$t_{\rm cool} \simeq 50 \left(\frac{v_{sh}}{300\ {\rm km\ s^{-1}}}\right)^{\alpha} \left(\frac{n}{0.01\ {\rm cm^{-3}}}\right)^{-1} {\rm Myr}, \quad (1)$$

for halo gas of subsolar metallicity $Z \simeq 0.2\ Z_\odot$ (Draine 2011; Kataoka et al. 2021), where $\alpha = 3.4$ at lower temperature than $kT \sim 1$ keV or velocity $v_{\rm sh} \sim 1000$ km s^{-1} and $\alpha = 1$ beyond. Assuming $v_{sh} \sim 1000$ km s^{-1} and $n \simeq 0.001$ cm^{-3} for front shock at high b, we obtain $t_{\rm cool} \simeq 1.5$ Gy that is much longer than dynamical scale for the bubbles' formation. Hence, the gas heated by front shock can be effectively adiabatic during the expansion.

The emissivity of the X-ray-emitting gas scales as $\propto n^2$, thus most of the observed emission comes from post-shock region rather than front shock, where $kT \simeq 0.3$ keV plasma dominates. The cooling time is then ~ 12 My, still long enough for the gas being regarded to be adiabatic.

The observed offset between radio and X-ray NPS is attributed to the position of the front shock and post-shock where the radio and X-ray emission becomes strongest. In fact, our MHD simulation (Sofue et al. 2016) predicts ~ 1 kpc offset at $z = 4$ kpc (or $b \simeq 30^\circ$) that corresponds to $\simeq 7^\circ$. This is roughly consistent with the observational radio/X-ray offset of $\simeq 5^\circ$ at the brightest part of the NPS (Kataoka et al. 2021).

2.3 Relieved X-ray maps and innermost X-ray spurs

In Fig. 4, we show a relieved map of soft X-ray intensity at 1–2.3 keV as produced from the eROSITA all sky map (Predehl et al. 2020). The relieving was applied by shifting the image in the longitude direction by a couple of angular resolution, then subtracting it from

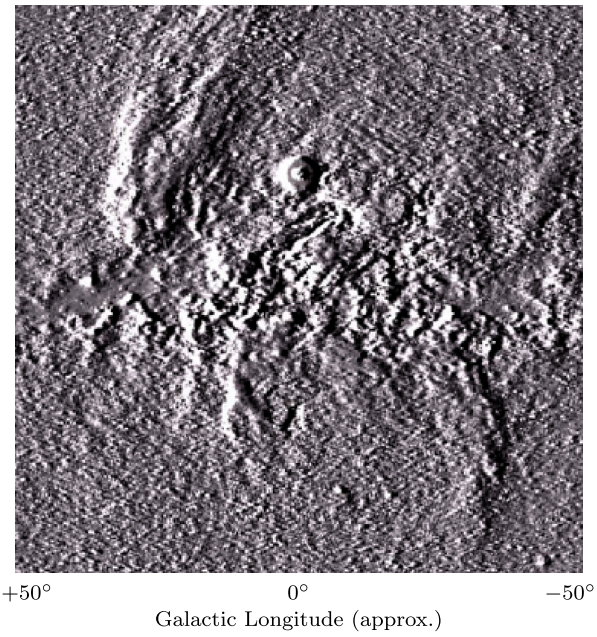

Figure 4. Relieved X-ray image produced from eROSITA all sky map at 1–2.3 keV using the colour image from Predehl et al. (2020).

the original image. By this simple procedure, the strong and relatively uniform galactic background is subtracted and small-scale structures are enhanced. Note, however, that the images may not be used for quantitative measurement of the intensity but is useful only for morphological study of the edged structures.

In the outer region at $|l| \sim >20^\circ$, X-ray spurs are coherently aligned along the radio spurs with significant displacements inside the bubbles (Kataoka et al. 2021). Symmetric to the North Polar Spur (NPS) with respect to the GC, a bright X-ray southern spur at ∼G−30−20, drawing a clear arc, is associated with the South Polar Spur West (SPS-W) in radio continuum. An X-ray spur at ∼G−30 + 20 is associated with the radio spur NPS-W, and the X-ray spur at ∼G+30−30 corresponds to SPS-E in radio. As a whole, both the radio and X-ray GSB compose an Ω/ʊ shape, making a symmetric dumbbell structure around the GC. Note, however, that they do not draw an eight-shape crossing at the nucleus. However, low-latitude extension below $|b| \sim <5^\circ$ of the X-ray spurs of the GSB and their connection to the Galactic disc at $l \sim \pm 20-30^\circ$ cannot be studied from the maps because of the strong absorption by the disc gas.

On the contrary, in a more central region at $|l| \sim <20^\circ$, we find numerous vertical X-ray structures, which include the near-GC spurs at G+10-05 (SE Claw) and G-05+05 (NW Clump; Kataoka et al. 2015) and the X-ray wind horns (Bland-Hawthorn & Cohen 2003). It is interesting to point out that these vertical features are located inside the H I wind cone. High-velocity ionized gas observed below the GC (Savage et al. 2017) could be related to these near-GC X-ray spurs.

2.4 Origin of energy injection: AGN or starburst?

The GC explosion model of the large-scale bubbles seems to be promising, but origin of energy injection is yet to be understood, either by an active galactic nuclei (AGN)-like outburst or from nuclear starburst in the GC. In general, AGN-like models assumes that energy is released as a single-point-like explosive event with a short time-scale in the nucelus, whereas starburst assumes that the energy is continuously released and injected to the GC over Myr time-scale. While the total amount of energy required is almost the same, AGN model predicts younger bubble ages of 1−3 Myr owing to fast expansion velocity of 1000–10 000 km s^{-1} (Guo & Mathews 2012). Such high velocity is apparently inconsistent with the observed X-ray temperature as discussed above, but situation can be significantly moderated by assuming constant AGN activity or continuous energy injection over Myr, leading to an expected plasma temperature of $kT \simeq 0.4$ keV (Zhang & Guo 2020).

In this context, starburst models more naturally explain observed X-ray temperature and overall morphology of bubbles owing to continuous star-forming activity over $\gtrsim$10 Myr (Sarkar et al. 2015; Sofue et al. 2016; Sarkar 2019). In this scenario, the shock velocity and temperature in the highest compression region in the post-shock wave is much smaller than that at the shock front by AGN models. The heated plasma can be gradually dissipated and/or cooled to form quasi-isothermal bubbles as observed in X-rays. However, it has been argued that the observed subsolar metallicity in the bubbles, $Z \simeq 0.2$ $Z_\odot$, seems to be difficult to be understood within the framework of starburst models (Inoue et al. 2015).

It seems that difference between AGN and starburst models simply depends on the energy injection time-scale, rather than physical origin itself. Thus, an alternative idea could explain the isothermal nature by assuming recurrent and continuous AGN activity as a source of energy injection over Myr time-scales. In fact, such recurrent activity are often observed in number of radio galaxies wherein multiple/mini radio lobes are found in quite different spatial size (e.g. Centaurus A: Israel 1998 for a review). The X-ray chimney, which looks like mini-bubbles, recently discovered in the GC is also collaborating this idea (Ponti et al. 2019). It is, however, difficult to clearly distinguish AGN and starburst scenario without detailed measurement of physical conditions of X-ray-emitting plasma, such as the gradient of temperature, metallicity, and ionization parameters against both latitude and longitude directions.

3 RADIO GSB INTERSECTING THE DISC

3.1 Radio bubbles

Fig. 5 shows a relieved image of radio continuum emission at 1420 MHz for a 100° × 100° region centred on the GC made from the Bonn-Stockert-Argentine all-sky survey (Reich et al. 2001). Almost identical features are observed in the relieved all-sky maps from the all-sky radio surveys at 408 MHz (Haslam et al. 1982) and 2300 MHz (Jonas, Baart & Nicolson 1998).

The north-eastern edge of the GSB, or the North Polar Spur (NPS), is visible as the brightest radio and X-ray ridge near $l = 30^\circ, b = +20^\circ$ (hereafter, G30+20). The western counterpart to NPS (NPS-W) is recognized near G-30+20 extending from the galactic plane to positive latitude. Their southern counterparts are recognized around G30-20 and G-30-20, which were called the South Polar Spurs East and West (SPS-E, SPS-W). These four spurs (NPS, NPS-W, SPS-E and SPS-W) compose a bipolar double-horn structure symmetric around the galactic plane and the rotation axis of the Galaxy.

3.2 Intersection with the galactic plane

The radio continuum spurs composing the GSB extend towards the galactic plane without significant absorption, and merge with the complex disc composed of numerous radio sources and extended structures. The northern radio spurs apparently stop at the Galactic plane, and appear to be connected to the southern spurs, although the details at $|b| \sim <1-2^\circ$ are not well established in the figures

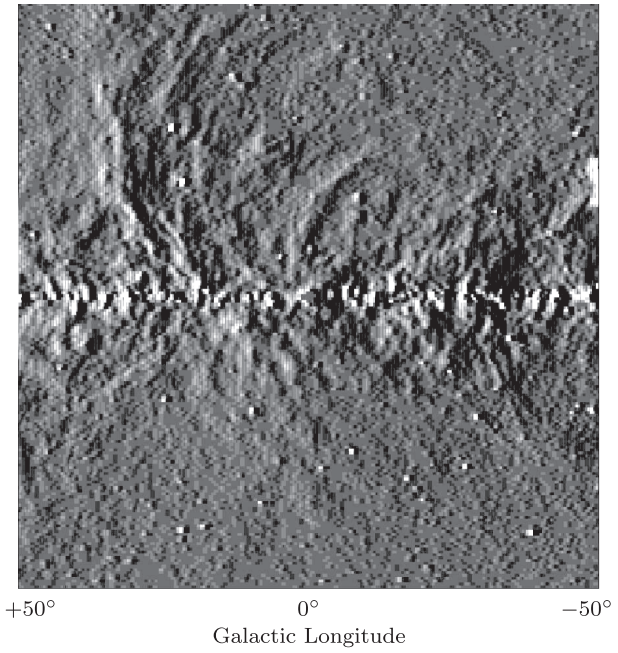

Figure 5. Horizontal-relieved map of 100° × 100° region around GC at 1420 MHz (Reich et al. 2001).

mainly because of the contamination by the fore- and background radio sources through the Galactic disc.

Among the spurs composing the GSB, the NPS is most prominent about the relation to the Galactic disc. The extension of the radio NPS towards the Galactic plane has been studied using background-filtered continuum maps observed with the Effelsberg 100-m telescope (Sofue & Reich 1979; Sofue (2000).

In order to see the intersection of NPS with the galactic plane in more detail, we show in Fig. 6 a relieved 2.8 GHz map made from the survey with the 100-m telescope at a resolution of 4′.3 (Reich et al. 1990) and relieved 4.8 GHz map from the Urmqi 25-m telescope at a resolution of 9′.5 (Sun et al. 2011). In the bottom panel, we show linearly polarized intensity map at 4.85 GHz (Sun et al. 2011), indicating that the spur's non-thermal nature of synchrotron origin. The polarization angle of the E vector along the spur lie at PA ∼ 130°, indicating that the B (magnetic) vector is at PA ∼ 40°, or the magnetic field is aligned along the spur, if the Faraday rotation is negligible.

At very low latitudes of $|b| \leq \sim 1°$, the radio continuum NPS, both in intensity and polarization, shows no signature of extension across the galactic plane. The fact that the NPS terminates at G21+01 at its brightest and sharpest end indicates that the NPS has its origin in the Galactic disc.

3.3 Magnetic fields

Besides the transparency for studying the morphological detail even through the galactic disc, an advantage to use radio continuum emission is its direct relation to the magnetic field in the shell.

If cosmic rays (CR) are produced by turbulent acceleration in the compression site of magnetic fields, we may assume equipartition between CR and magnetic energy densities. Then, the magnetic strength can be estimated using the relation (Sofue, Nakanishi & Ichiki 2019)

$$B \sim 3.1 \times 10^8 (\nu/1\ \mathrm{GHz})^{-1/7} \epsilon^{2/7}\ \mu\mathrm{G}, \qquad (2)$$

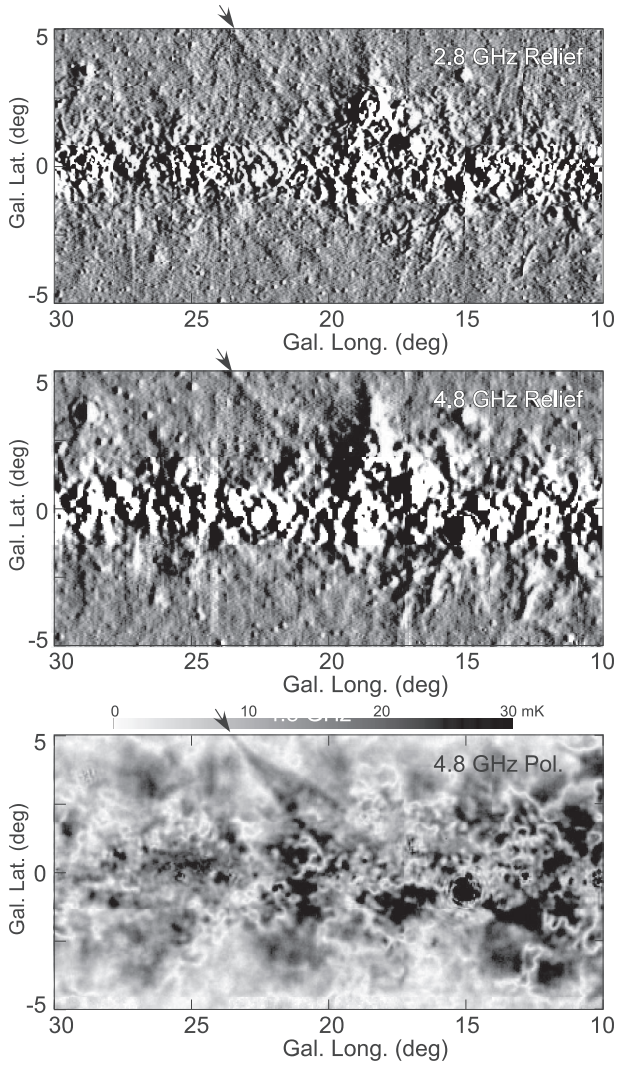

Figure 6. [Top] 2.8 GHz relief map from Bonn 100-m telescope survey (Reich et al. 1990) near the root of the NPS. The arrows points the extension of the NPS. [Middle] 4.8 GHz relief from Urmqi 25-m telescope survey (Sun et al. 2011). [Bottom] Same, but polarized intensity. Arrows point the NPS ridge. A bright source at ∼G19+03 is a foreground HII region, which is not visible in polarization.

where ν [in GHz] is the radio frequency and $\epsilon = 4\pi \int \Sigma_\nu d\nu / L \sim 4\pi \nu \Sigma_\nu / L$ [in erg cm^{-3} s^{-1}] is the radio emissivity for line-of-sight depth L of the emission region. Here, $\Sigma_\nu = 2kT_{\mathrm{B}\nu}/\lambda^2$ is radio surface brightness at ν, $T_{\mathrm{B}\nu}$ the brightness temperature, and λ the wavelength.

Inserting observed excess in brightness temperature of $T_\mathrm{B} \sim 0.5$ K at 2.3 GHz (Jonas et al. 1998), ∼1.4 K at 1.4 GHz (Reich et al. 2001), and ∼40 K at 408 MHz (Haslam et al. 1982) towards the NPS ridge at $b \sim 30°$, we obtain volume emissivity of $\epsilon \sim 1.5 \times 10^{-29}$, $\sim 0.96 \times 10^{-29}$, and $\sim 0.68 \times 10^{-29}$ erg cm^{-3} s^{-1}, respectively. These values yield magnetic strength of $B \sim 1.6\ \mu$G for an assumed line-of-sight depth of $L \sim 0.5$ kpc. Then, the magnetic energy density, which is equal to CR energy density, is $u_\mathrm{mag} = u_\mathrm{CR} \sim B^2/8\pi \sim 1.0 \times 10^{-13}$ erg cm^{-3}. This is smaller than that of the X-ray-emitting thermal gas with $kT \sim 0.3$ keV and $n \sim 10^{-2}$ cm^{-3}, having $u_\mathrm{thermal} \sim 5 \times 10^{-12}$ erg cm^{-3}. The decay time of CR electrons emitting at 1.4 GHz is estimated to be $t_{\mathrm{CR\,decay}} \sim u_\mathrm{CR}/\epsilon \sim 0.4$ Gy. This is longer

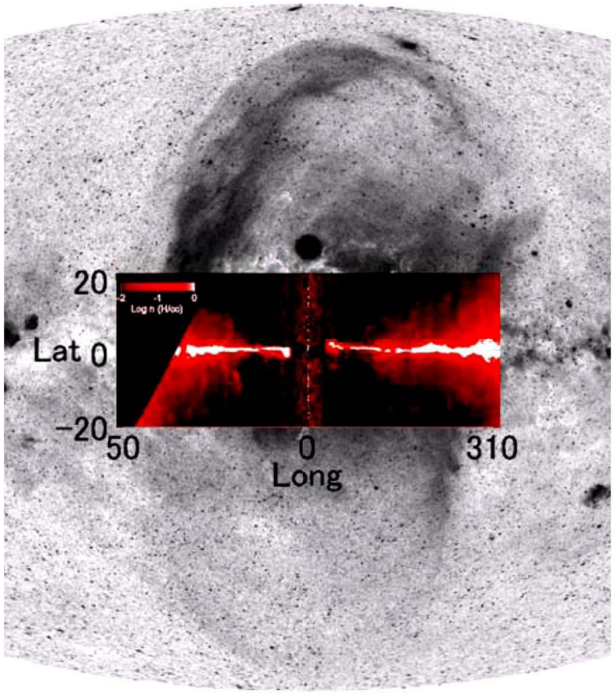

Figure 7. X-ray image by eROSITA (Predehl et al. 2020) at 1–2.3 keV compared with H I volume density ($n_{\rm H\,I} \propto T_{\rm B}$) at tangent velocities, showing the cylindrical cavity coincident with the bubbles (Sofue 2017).

than the dynamical time of the shock wave, $t_{\rm dyn} \sim 10$ My, but shorter than the cooling time of the thermal gas, $t_{\rm cool} \sim 1.5$ Gy.

It is noted that much more energy may be reserved in CR protons rather than electrons, but the emission from CR protons are hard to be observed. In fact, recent MHD simulation on the SNR shock suggests that energy density in the CR protons is several orders of magnitude larger than that of CR electrons, depending on the SNR age in Sedov phase (Urosević et al. 2018). Moreover, given that only a small fraction of cold protons are picked up into the CR acceleration process, we should also consider hidden contribution of *cold* protons as a reservoir of CR protons. Thus, the substantial mismatch between CR electrons, magnetic fields, and X-ray-emitting gas may suggest that most of energy may be stored by protons in the front shock of the NPS and GSBs.

Morphological comparison between X-ray and radio spurs on the sky has posed an interesting question about the displacement between the X-ray and radio edges, such that the X-ray shell is located significantly inside the radio shell (Kataoka et al. 2021). The large displacement may imply either that the frozen-in nature does not hold between the gas and magnetic fields in the GSB. Alternatively, the acceleration of CR electrons is local and their lifetime is comparable with the GSB's evolutionary time-scale, which is, however, marginal in view of the lifetime estimation in Section 4.3.

4 3-KPC CRATER AS A FOOTPRINT BY GSB ON THE DISC

4.1 GSB's root enveloped by H I hole and 3-kpc crater

We first overview the spatial relation of the GSB to the H I hole and 3-kpc crater in the Galactic disc and halo (Lockman 1984; Lockman & McClure-Griffiths 2016; Sofue 2017). In Fig. 7, we overlaid a map of the H I volume density ($n_{\rm H\,I} \propto T_{\rm B}$) along the terminal velocity circle made from GASS H I survey (McClure-Griffiths et al. 2009) on the eROSITA X-ray map (Predehl et al. 2020). The low-latitude X-ray spurs composing the GSB approximately coincide in position with the inner wall of the H I hole (conical cavity). The inner H I disc is as thin as $\sim 1^\circ$ inside 3 kpc, but the disc suddenly becomes thicker and denser at $l \sim 22^\circ$, attaining a thickness of $\sim 10^\circ$, exhibiting a crater structure. The H I wall composes vertical spurs extending to $b \sim \pm 10^\circ$ (1 kpc), coinciding also with the radio spurs. These facts agree with the idea that the NPS and its counter spurs compose a dumbbell-shaped shock front, which swept away the interior H I disc inside $\sim$3 kpc.

4.2 Longitude-velocity diagrams

Fig. 8 shows H I line longitude–velocity (LV) diagrams made from the Parkes All Sky Survey (GASS) of the H I line emission (McClure-Griffiths et al. 2009) at $b = 0^\circ$ and $0.^\circ 6$. The 3-kpc-expanding ring (H I crater's wall) is evident as the tilted ellipse of H I ridge in the LV diagram, which crosses $l = 0^\circ$ at positive and negative high velocities of $\pm 50 - 60$ km s^{-1}.

The negative velocity (approaching) arm is recognized at $b \sim \pm 0.^\circ 5 - 0.^\circ 6$ both in CO and H I LVDs, while positive velocity arm is fainter at $\pm 0.^\circ 5$. In the off-plane regions at $b = \pm 0.^\circ 5 - 0.^\circ 6$ at $|l| \sim \leq \sim 20^\circ$, there appears a vacant region of tangent-velocity gases, marked as H I hole. Such an LV behaviour implies that the gases are empty inside 3 kpc at these latitudes.

Fig. 9 shows LV diagrams of the ^{12}CO(J = 1−0) emission at higher resolution from the FUGIN[2] (Umemoto et al. 2017) CO survey around the northern tangent point of the 3-kpc ring. The figure indicates that the upper layer of the molecular disc is sharply truncated at $b \sim 0.^\circ 5$ (65 pc).

4.3 Explosion versus bar origin

The non-circular motion exhibited by the elliptical feature in the LV diagram in the 3-kpc arm has been interpreted in two ways.

One idea is that the ring is expanding, accelerated by an explosion at the GC (Sanders & Prendergast 1974; Bania 1980; Sofue 1984). The gas is approaching to the Sun in the near side at negative radial velocity of -53 km s^{-1}, while receding in the far side at positive velocity at $+56$ km s^{-1} (Dame & Thaddeus 2008). This motion produces a simple LV ellipse, as shown by the dashed line in Fig. 8, which reasonably traces the observed H I LV ellipse. The total mass of the CO and H I rings is on the order of $\sim 10^8$ M$_\odot$, and their kinetic energy of the expanding motion at 50 km s^{-1}is $\sim 5 \times 10^{54}$ erg (Sofue 2017). This requires only a small portion, $\sim$0.1, of the total energy to drive the ring's expansion. The angular momentum problem may be eased, if the ring is a focusing wave front and not an accumulated ring Sofue (1977).

Another idea is that the non-circular LV feature is produced by a bar potential Weinberg (1992) according to the various families of 'x' orbits (Contopoulos 1956). Simulations have shown complicated LV features, known as the parallelogram, whose orientation depends on the position angle, mass, axial lengths, and ratio of the bar in a complex way (Binney et al. 1991; Athanassoula & Bureau 1999; Sormani, Binney & Magorrian 2015).

We may also combine the two ideas in such a way that the halo structures are produced by the explosion, while the disc's LV feature

[2]Four-receiver system Unbiased Galactic Imaging survey with the Nobeyama 45-m telescope.

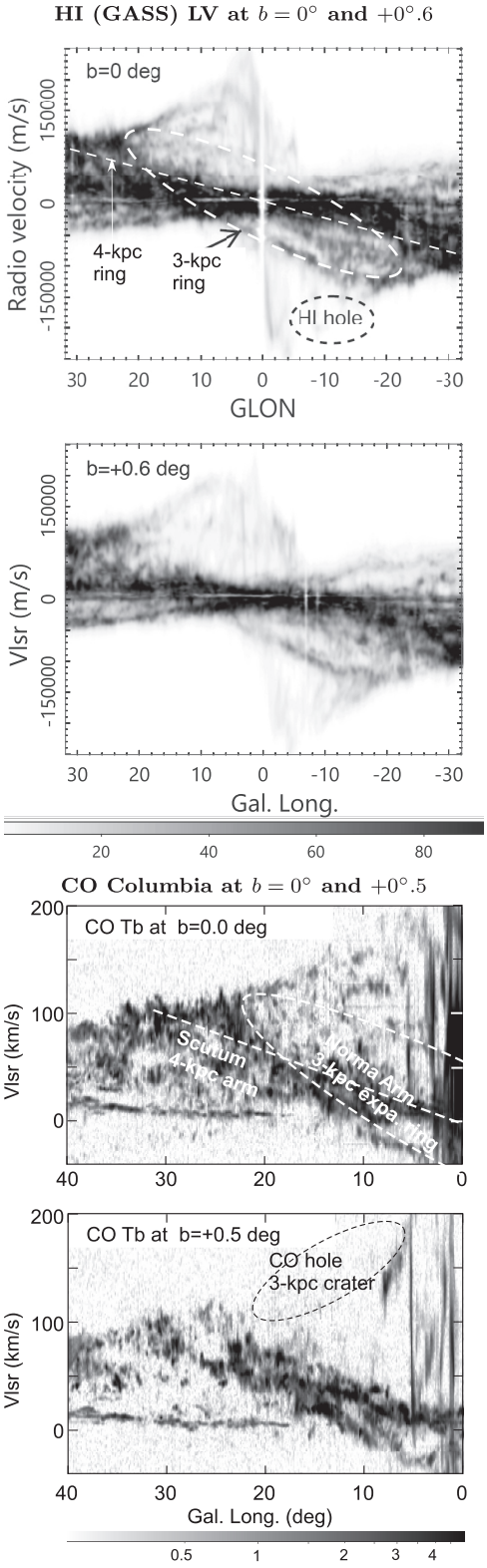

Figure 8. LV diagrams in the H I line at $b = 0°$ and $+0.6°$ from GASS survey (McClure-Griffiths et al. 2009), and CO line at $b = 0°$ and $+0°.5$ from Colombia survey (Dame, Hartman & Thaddeus 2001) . The 3-kpc-expanding ring is indicated by the dashed ellipse.

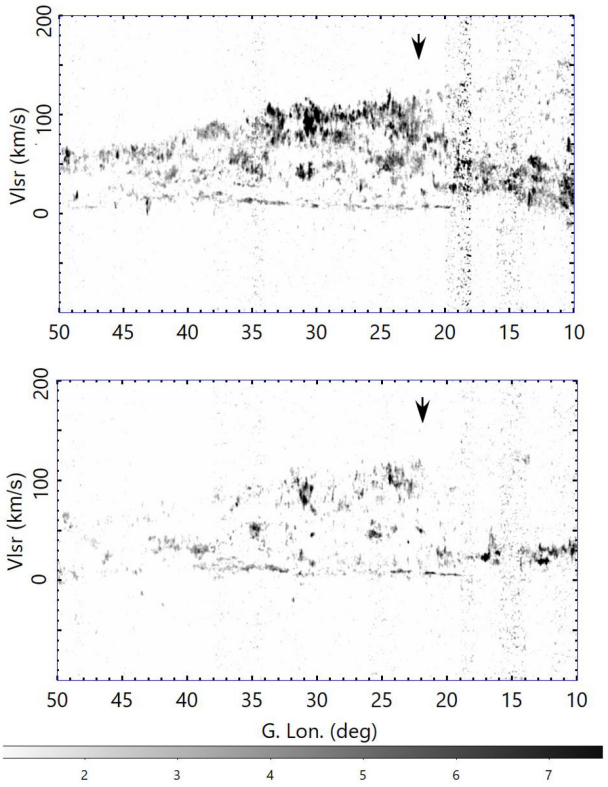

Figure 9. CO-line LV diagrams at $b = +0°$ (top) and $0°.5$ (bottom) from the FUGIN survey (Umemoto et al. 2017). Note the clear cut-off terminal-velocity clouds at $l = 22°$ as indicated by the arrows.

by the bar. The bar promotes accretion of the disc gas to GC, and triggers starburst and/or AGN, producing the GSB. However, in this case, we must assume that (1) the exact coincidence of the 3 kpc arm with the roots of GSB and H I cylinder happened by chance, (2) the gigantic explosion did not give any imprint on the disc, and (3) the bar and flow orientation must be special to produce the observed simple LV oval.

Considering these, particularly the fact that the observed 3-kpc LV oval is fitted by a simple ellipse fairly well as in Fig. 8, not particularly requiring a parallelogram, we here attempt to explain the GSB, H I cylinder, 3-kpc ring, and the H I+CO crater structure by a single hypothesis of the GC explosion. Note that the explosion model explains the 3D structures in the halo and disc, whereas the current bar simulations cannot touch upon the vertical structures. A more sophisticated 3D model incorporating a bar and GC blast would be desirable, although it is beyond the scope of this paper.

4.4 Density and disc thickness jumps at 3-kpc crater

Fig. 10 shows longitudinal variations of the H I and CO line brightness temperatures T_B at the tangent-point velocities plotted against longitude in the galactic plane and at $b = \pm 0°.5 - 0°.6$. We recall that T_B is proportional to the mean volume density in the line-of-sight depth through the tangent point gas as

$$n_i = \frac{dN_i}{dx} = \frac{dN_i}{dv}\frac{dv}{dx} = X_i T_B \frac{dv}{dx}, \quad (3)$$

where $i =$ H I or CO with X_i being the conversion factors, x and v the distance along the line of sight and radial velocity, respectively.

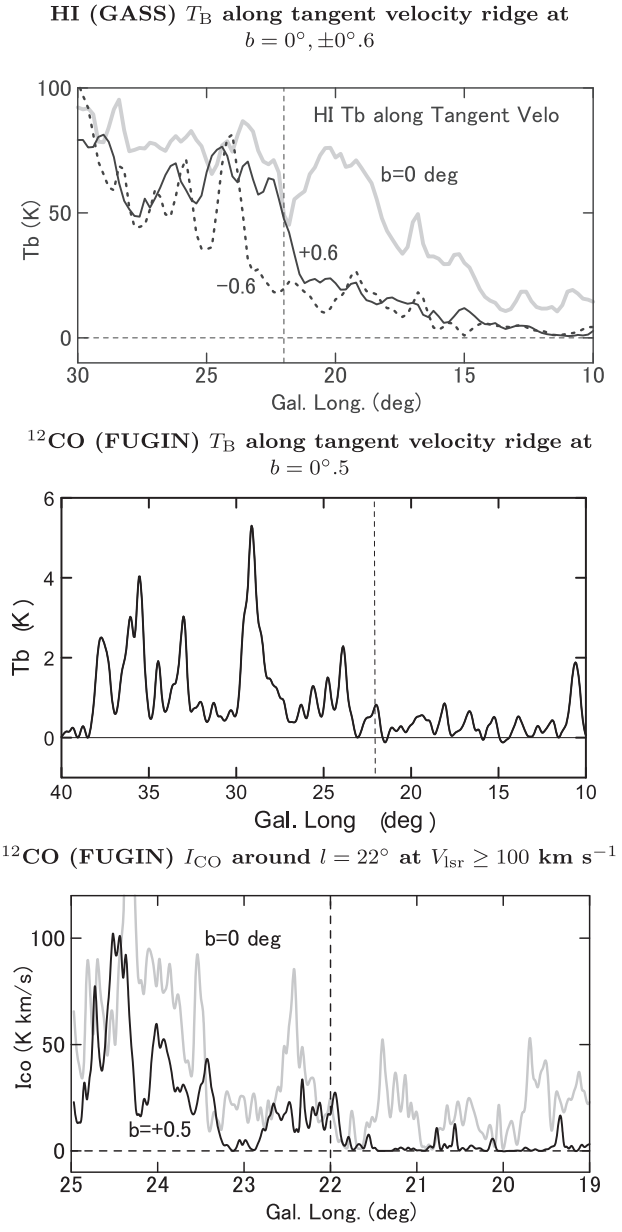

Figure 10. [Top] Longitudinal variation of T_B of H I gas (GASS) at tangent points at different latitudes, $b = 0°$ and $\pm 0°.6$($\pm$78 pc). [Middle] FUGIN ^{12}CO(J = 1−0)T_B at tangent points at $b = +0°.5$ (+65 pc). [Bottom] FUGIN ^{12}CO($J = 1-0$)intensity at $V_{lsr} \geq 100$ km s^{-1}at $b = 0°$ and $0°.5$ $z = +65$ pc. Note the jump of the gas density at $l \sim 22°$ corresponding to the 3-kpc crater, within which the H I and CO gas discs are truncated.

The velocity gradient is on the order of dv/d$x \sim 5$ km s^{-1} kpc^{-1} for a velocity gradient of $\sim$5 km s^{-1}and a line-of-sight depth across the tangent-velocity gas of $\sim$1 kpc. For H I with $X_{HI} = 1.8 \times 10^{18}$ H cm^{-3} [K km s^{-1}]$^{-1}$ and $T_B \sim 80$ K, we obtain a mean density of $n_{HI} \sim 0.3$ H cm^{-3}. For CO with $X_{CO} \sim 2 \times 10^{20}$ H$_2$ cm^{-2} [K km s^{-1}]$^{-1}$ and $T_B \sim 5$ K, we obtain $n_{H_2} \sim 2$ H$_2$ cm^{-3}.

The T_B plots in Fig. 10 show a step-like increase of the volume densities of H I and CO gas from lower to higher longitudes at $l = 22°$. In the Galactic plane ($b = 0°$), the density jump of the molecular gas takes place from a finite but small value inside 22° to higher values. On the other hand, the off-plane molecular gas is almost empty inside =22°, but suddenly attains finite values beyond this longitude. Such a

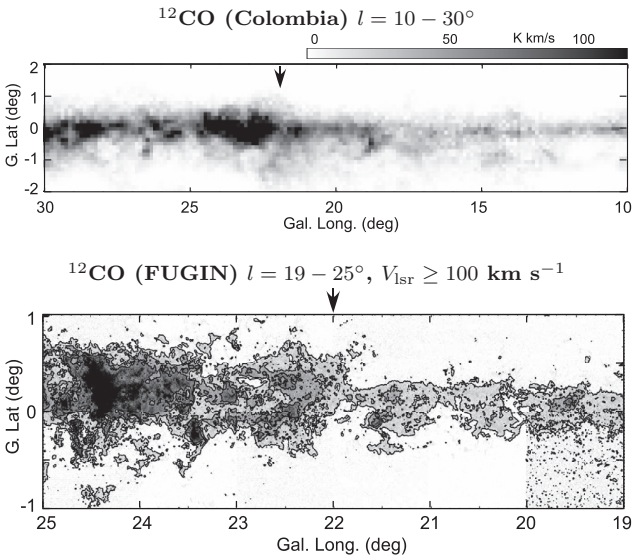

Figure 11. [Top] ^{12}CO(J = 1−0)I_{CO} maps integrated at $V_{lsr} \geq 60$ km s^{-1} from Columbia survey (top), and [Bottom] I_{CO} from FUGIN survey integrated at $V_{lsr} \geq 100$ km s^{-1}. Contours are at 10, 30, and 50 K km s^{-1}. Note the step-like increase of the disc thickness at $l \sim 22°$ as traced by the lowest contours, indicating truncation of the upper layer inside 3 kpc.

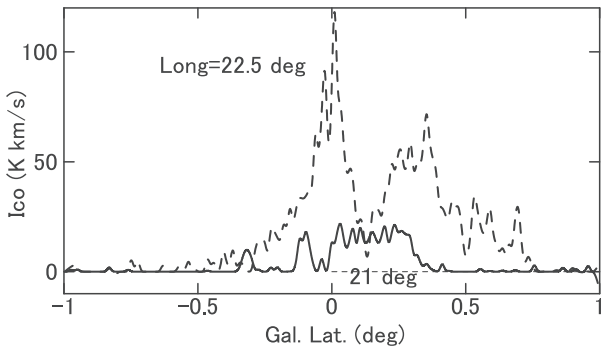

Figure 12. Latitude cross-sections of I_{CO} ($V_{lsr} \geq 60$ km s^{-1}) at G21 and G22.5 around the 3-kpc ring from FUGIN, showing drastic change of the vertical extent of the molecular disc from inside to outside the 3 kpc ring at $l = 22°$.

density profile indicates that the molecular gas disc is thin inside 22°, and is surrounded by a thicker disc beyond the longitude, making a wall-like distribution with a radius of 3 kpc.

Cross-section of the gas distribution in the 3-kpc crater can be more directly displayed by channel maps in the H I and CO-line emissions at the terminal velocity. Fig. 11 shows I_{CO} maps integrated at $V_{lsr} \geq 60$ km s^{-1} from the Columbia CO survey, and the same but at $V_{lsr} \geq 100$ km s^{-1}from the Nobeyama FUGIN survey around $l \sim 22°$. A sudden jump of the thickness of CO disc is recognized at $l = 22°$ such that the thickness by full width at at half-maximum) of $\sim 0°.5$ at $l \leq 22°$ to $\sim 1°.5$ at $l > 22°$.

The sudden change of the thickness revealed in the FUGIN CO map suggests that the upper layer of the molecular disc has been sharply truncated by sweeping mechanism inside $l \leq 22°$ due to a shock wave from the GC or a horizontal wind blowing in the halo.

The thickness variation may be more clearly seen by comparing vertical cross-sections at different longitudes outside and inside of the 3-kpc arm at G22. Fig. 12 shows the cross-section at G22.5

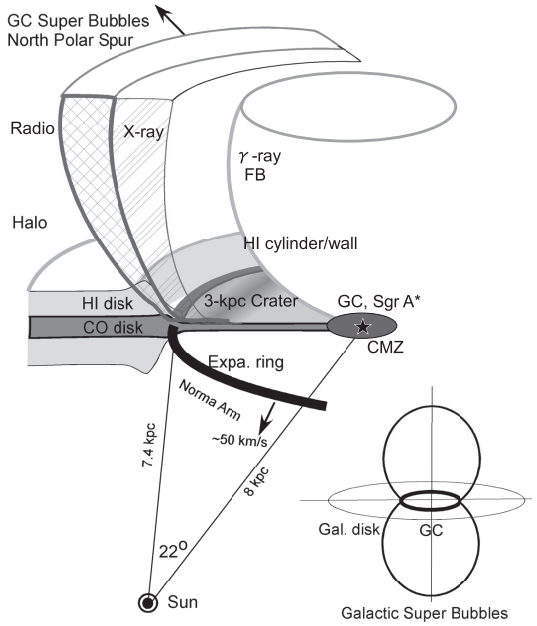

Figure 13. Schematic illustration of the relation of GSB (NPS) to the GC and 3-kpc-expanding ring (Norma Arm) and crater.

compared with that at G21. The former shows a wide extent of the disc, having an outskirt to high latitudes. On the other hand, the cross-section at G21 shows a plateau-like distribution, sharply cut at $\pm 0^\circ.25$ from the centroid, suggesting truncation of the outskirt.

Thus, the horizontal (longitudinal) and vertical (latitudinal) variations show that the density and thickness of the galactic gas disc, both in H I and CO, increase suddenly at $l \sim 22^\circ$. The variation is more step-like in the off-plane region at $|b| \sim 0^\circ.5$ than in the galactic plane.

From Fig. 12, the molecular disc thickness inside G22 is as thin as $\pm 0^\circ.25$ (30 pc) and increases to $\sim 1^\circ$ outside 22°. This indicates that the galactic disc of neutral gas (H I and CO) has a crater structure, having a hole inside G22 above the disc at $|z| > \sim 30$ pc ($0^\circ.25$). As shown in Fig. 10, the H I hole's wall has a radius of $r = 3$ kpc and thickness ~ 260 pc (rising full width of $\sim 2^\circ$ measured at $b = 0^\circ.6$). On the other hand, the CO hole has a much sharper wall with thickness of ~ 30 pc ($\sim 0^\circ.2$ at $b = 0^\circ.5$).

4.5 Formation of the crater and energetics

It has been shown that the root of the GSB can be traced by radio continuum ridges intersecting the Galactic plane. The NPS root was shown to exactly coincide with the 3-kpc-expanding ring composed of H I and molecular gases. Fig. 13 illustrates a schematic view of the interaction of the GSB with the H I and CO disc based on the observed data shown in the previous subsections. In the upper halo, the GSB makes giant shells with the radio continuum being located outside X-rays (Kataoka et al. (2021), and is enveloping the γ-ray bubble (Su et al. 2010). The upper layer of the galactic disc is swept away and accumulated in the wall of the 3-kpc crater, creating the H I and CO rings. By the focusing effect of the shock wave on the disc (Sofue 1977, 2020), the front near the disc makes a compressed ring with the expansion velocity at $\sim 50\,\mathrm{km\,s^{-1}}$. However, the thin and densest area near the Galactic plane at $|b| \lesssim 1^\circ$ remains almost unperturbed because of the rapid deceleration of the shock wave in the plane inside 1–2 kpc from the GC.

Using the observed brightness temperatures and three-dimensional distribution expected from the apparent extent on the sky and assumed distance, the mass of the 3-kpc ring has been estimated to be $1.5 \times 10^8\,M_\odot$ Sofue (2017). The corresponding kinetic energy is estimated to be on the order of $\sim 5 \times 10^{54}$ erg for the expanding motion at $50\,\mathrm{km\,s^{-1}}$ (Sofue 2017). This energy is an order of magnitude smaller than the currently estimated total energy required for the formation of the GSB of $\sim 10^{55-56}$ erg. Hence, energetically, it is reasonable to assume a common origin for the formation of the GSB and the 3-kpc-expanding ring with the H I and CO crater in the galactic disc.

5 DISCUSSION

5.1 Unified view of the GSB in X, radio, H I, and CO

We have re-visited the GSB using the all-sky X-ray and radio continuum surveys as well as H I and the newest CO-line data of the galactic disc. From the wide coverage of the observed energy ranges as well as by the spectral line information, we are now able to obtain a unified view of the GSBs as follows.

The X-ray data are crucial to derive thermal and kinematic properties of the GSB as a shock wave from the GC propagating through the halo gas. Gaseous temperature can be used to calculate the shock wave velocity v, which is related to the injection energy E_0 at the GC and accumulated total mass M of the shell by $E_0 \sim 1/2Mv^2$ for an adiabatic shock wave as reasonably assumed from the sufficiently long cooling time. From X-ray spectroscopy, we know that $kT \sim 0.3$ keV (Fig. 3), and the intensity yields thermal electron density on the order of $n \sim 10^{-2}\,\mathrm{cm^{-3}}$ for assumed radius ~ 4 kpc and thickness ~ 1 kpc. These estimations lead to $M \sim 2 \times 10^8 M_\odot$ and $E_0 \sim 4 \times 10^{55}$ erg. Under the adiabatic assumption, the age of the GSB is approximately estimated from the current expansion velocity as $t \sim 0.6r/v \sim 11$ My.

Although X-ray data are useful for discussing the shock wave propagation and energetics, they strongly suffer from the interstellar extinction by heavy elements in the galactic disc, where the optical depth steeply increases towards the galactic plane as $\propto \sec |b|$. This results in the dark absorption belt along the galactic plane in the all-sky X-ray maps, making it difficult to obtain information about the interaction of the high-temperature gas with the galactic disc.

Such difficulty can be eased by observing radio continuum emission that can be safely assumed to be transparent in the whole Galaxy including the disc. We have thus showed that the roots of the GSB are connected to the tangential directions of the 3-kpc-expanding ring as revealed in the H I and CO line emissions.

The radio ridge of the NPS was shown to be extending straightly towards the galactic plane, getting sharper and brighter and terminating at $b \sim 1^\circ$ after merging into the bright disc emission. From the intersection of the GSBs' spurs at longitudes of $\sim \pm 20^\circ$, we showed that the whole GSB structure composes an Ω/ ʊ shape.

The distribution of H I and molecular gases along the tangent-velocity circle showed that the ring composes a crater-like structure in the disc around the GC. The 3-kpc ring and crater wall are expanding at $\sim 50\,\mathrm{km\,s^{-1}}$ as inferred from the LV diagrams. Kinetic energy of the expanding motion of the ring is estimated to be on the order of 5×10^{54} erg. Namely, a small portion of the total energy required to drive the whole GSB (10^{55-56} erg) is sufficient to drive the expanding ring and to create the crater.

We emphasize that the GC explosion model explains the coherent 3D structures in the disc and halo around 3 kpc, which include the sudden increase in the disc thickness at $l \sim 22^\circ$ beyond horizontal

truncation of the upper layer inside 3 kpc and the cylindrical H I wall around the central cavity as well as the non-circular kinematics revealed in the LV digrams.

5.2 Galactic-scale feedback

Finally, we will comment on the implications of the interaction between the GSB and the galactic disc, assuming that the expanding ring of the gas disc is due to a GC explosion. Current research of GSB in the literature has been devoted to discussing its impact on the galactic halo. However, in the following we highlight the impact on the disc and its activity. This may somehow akin to discussing the impact of an explosion on the earth not only on the atmosphere, but also on structures on the ground.

The shock wave velocity is variable with the gaseous density in such a way that the velocity decreases with the density. Accordingly, the ray path of a wave is refracted due to varying propagation velocity in the disc and halo. This causes a converging flow of the shock front towards the galactic disc, making a ring of focusing waves Sofue (2020).

If the wave amplitude is small enough, or it is a linear wave like sound and MHD waves, the focal length f is approximately related to the scale height of the disc h as $f \sim 2.2\,h$ Sofue (1977), Sofue (2020). Thus, besides the large-scale energetic flow as huge bubbles into the halo, some fraction of the released energy at the GC propagates the galactic disc and lower halo, repeating focusing on to rings of radii $r_i \sim 2.2\,I\,h$ with $i = 1, 2, ...$

The 3-kpc ring could be one of such focal rings driven by the GC activity, although its amplitude is non-linear and the simple focusing law may not apply and the focal length would be longer than $2.2\,h$. Also, after passing a focal ring, the wave diverges again into the disc and halo, propagates further outward, repeating focusing.

It is therefore expected that some fraction of the released energy at the GC by starburst or AGN activity is efficiently confined in the disc and lower halo, and repeat convergence on to disc-wide focal rings. We emphasize that, besides the GSB's effects on the halo and intergalactic space, the galactic-scale feedback of the GC activities back on to the disc is also important for considering the structure and evolution of the Galaxy (Sofue 2020). For example, convergence of the released energy from the GC, even though a fraction of the total amounting to $\sim 10^{55-56}$ erg per $\sim$10 My, would cause various dynamical effects in the disc, which include triggering of star formation by compression in focal rings, and generation of the interstellar turbulence.

6 SUMMARY

We revisited the GSBs, being inspired by the eROSITA all-sky X-ray observations (Predehl et al. 2020), and discussed their origin as due to an explosion in the Galactic centre. With a particular emphasis of the interaction of the bubbles with the Galactic disc, we investigated the radio continuum, X-rays, H I surveys, and the newest high-resolution CO-line survey of the Galactic disc. We showed that the roots of the bubbles coincide with the 3-kpc-expanding ring and crater in the H I and CO discs of the Galaxy. They thus revealed 3D structure of the crater is explained by sweeping of the disc gas by the GSB as a footprint of the explosive event in the Galactic centre. The origin of the GSB can be well modelled by a Ω/ ℧ shaped shock wave from the GC with an explosive energy input of several 10^{55} erg $\sim$10 My ago.

DATA AVAILABIVITY

The CO line data were taken from the FUGIN CO-line survey at url: https://nro-fugin.github.io/. The eROSITA X-ray image was taken from the url: https://www.mpe.mpg.de/7461761/news20200619.

ACKNOWLEDGEMENTS

The authors are indebted to Prof. A. Habe for the hydrodynamical simulation for Fig. 1 as reproduced from our paper in 2016. JK acknowledges the support from JSPS KAKENHI Grant Number JP20K20923.

REFERENCES

Akita M., Kataoka J., Arimoto M.,Yoshiaki S.,Tomonori T.,Yoshiyuki I.,Nakashima S.,2018, ApJ, 862, 88
Athanassoula E., Bureau M., 1999, ApJ, 522, 699
Bania T. M., 1980, ApJ, 242, 95
Binney J., Gerhard O. E., Stark A. A., Bally J., Uchida K. I., 1991, MNRAS, 252, 210
Bland-Hawthorn J., Cohen M., 2003, ApJ, 582, 246
Carretti E. et al., 2013, Nature, 493, 66
Cohen R. J., Davies R. D., 1976, MNRAS, 175, 1
Contopoulos G., 1956, ApJ, 124, 643
Crocker R. M., Bicknell G. V., Taylor A. M., Carretti E., 2015, ApJ, 808, 107
Dame T. M., Thaddeus P., 2008, ApJ, 683, L143
Dame T. M., Hartman D., Thaddeus P., 2001, ApJ, 547, 792.
Draine B. T., 2011, Physics of the Interstellar, Intergalactic Medium, Princeton University Press
Guo F., Mathews W. G., 2012, ApJ, 756, 181
Haslam C. G. T., Salter C. J., Stoffel H., Wilson W. E., 1982, A&A, 47, 1
Heywood I. et al., 2019, Nature, 573, 235
Inoue Y., Nakashima S., Tahara M.,Kataoka J.,Totani T.,Fujita Y.,Sofue Y.,2015, PASJ, 67, 56
Israel F. P., 1998, A&AR, 8, 237
Jonas J. L., Baart E. E., Nicolson G. D., 1998, MNRAS, 297, 977
Kalberla P. M. W., Burton W. B., Hartmann D.,Arnal E. M.,Bajaja E.,Morras R.,Pöppel W. G. L.,2005, A&A, 440, 775
Kataoka J. et al., 2013, ApJ, 779, 57
Kataoka J., Tahara M., Totani T.,Sofue Y.,Inoue Y.,Nakashima S.,Cheung C. C.,2015, ApJ, 807, 77
Kataoka J., Sofue Y., Inoue Y., Akita M., Nakashima S., Totani T., 2018, Galaxies, 6, 27
Kataoka J., Yamamoto M., Nakamura Y.,Ito S.,Sofue Y.,Inoue Y.,Nakamori T.,Totani T.,2021, ApJ, 908, 14
Lallement R., Snowden S., Kuntz K. D.,Dame T. M.,Koutroumpa D.,Grenier I.,Casandjian J. M.,2016, A&A, 595, A131
LaRocca D. M., Kaaret P., Kuntz K. D.,Hodges-Kluck E.,Zajczyk A.,Bluem J.,Ringuette R.,Jahoda K. M.,2020, ApJ, 904, L54
Lockman F. J., 1984, ApJ, 283, 90
Lockman F. J., McClure-Griffiths N. M., 2016, ApJ, 826, 215
McClure-Griffiths N. M. et al., 2009, ApJS, 181, 398
Miller J. M., Bregman J. N., 2016, ApJ, 829, 9
Nakashima S., Nobukawa M., Uchida H.,Tanaka T.,Tsuru T. G.,Koyama K.,Murakami H.,Uchiyama H.,2013, ApJ, 773, 20
Planck collaboration IX, 2013, A&A, 554, 139
Ponti G. et al., 2019, Nature, 567, 347
Ponti G., Morris M. R., Churazov E.,Heywood I.,Fender R. P.,2021, A&A, 646,A66
Predehl P. et al., 2020, Nature, 588, 227
Reich W., Fuerst E., Reich P., Reif K., 1990, A&AS, 85, 633
Reich P., Testori J. C., Reich W., 2001, A&A, 376, 861
Sanders R. H., Prendergast K. H., 1974, ApJ, 188, 489
Sarkar K. C., 2019, MNRAS, 482, 4813
Sarkar K. C., Nath B. B., Sharma P., 2015, MNRAS, 453, 3827
Savage B. D. et al., 2017, ApJS, 232, 25

Snowden S. L. et al., 1997, ApJ, 485, 125
Sofue Y., 1977, A&A, 60, 327
Sofue Y., 1980, PASJ, 32, 79
Sofue Y., 1984, PASJ, 36, 539
Sofue Y., 1994, ApJ, 431, L91
Sofue Y., 2000, ApJ, 540, 224
Sofue Y., 2015, MNRAS, 447, 3824
Sofue Y., 2017, PASJ, 69, L8
Sofue Y., 2020, MNRAS, 498, 1335
Sofue Y., Handa T., 1984, Nature, 310, 568
Sofue Y., Reich W., 1979, AAS, 38, 251
Sofue Y., Habe A., Kataoka J., Totani T., Inoue Y., Nakashima S., Matsui H., Akita M., 2016, MNRAS, 459, 108
Sofue Y., Nakanishi H., Ichiki K., 2019, MNRAS, 485, 924
Sormani M. C., Binney J., Magorrian J., 2015, MNRAS, 454, 1818
Su M., Slatyer T. R., Finkbeiner D. P., 2010, ApJ, 724, 1044
Sun X. H., Reich W., Han J. L., Reich P., Wielebinski R., Wang C., Müller P., 2011, A&A, 527, A74
Tahara M. et al., 2015, ApJ, 802, 91
Umemoto T. et al., 2017, PASJ, 69, 78
Urosević D., Pavlović M. Z., Arbutina B., 2018, ApJ, 855, 59
Weinberg M. D., 1992, ApJ, 384, 81
Zhang R., Guo F., 2020, ApJ, 894, 117

This paper has been typeset from a TEX/LATEX file prepared by the author.